European Journal of Mechanics B/Fluids 28 (2009) 613–618

Contents lists available at ScienceDirect

European Journal of Mechanics B/Fluids

journal homepage: www.elsevier.com/locate/ejmflu

Shock propagation along a two-layer interface in confined geometry

R. Piron, P. Ballereau, B. Canaud*

CEA, DAM, DIF, F-91297 Arpajon, France

ARTICLE INFO

Article history:
Received 20 October 2008
Received in revised form
6 April 2009
Accepted 7 April 2009
Available online 18 April 2009

PACS:
52.57.Bc
52.35.Tc
52.35.We

Keywords:
Shock propagation
Shock irregular refraction
Vorticity sheet

ABSTRACT

The paper presents direct numerical simulations of the propagation of a strong planar shock wave along a two-layer interface confined between two walls. Transient stage and steady state of the propagation are described. In the steady state regime, a stationary irregular refraction of the shock and a vorticity sheet are characterized. Physics of the stationary irregular refraction state is explained. Shock velocity is studied. Quantities are shown to verify a set of generalized Rankine–Hugoniot relations. The unknown coupling mechanism between shear layer and pressure step is predicted by a neural network which leads to a predictive, gray-box type model.

1. Introduction

Strong shock propagation in a non-homogeneous medium is of basic interest for many physical fields from laser fusion to astrophysics. In Direct-Drive Inertial Confinement Fusion [1] (ICF), some target designs propose the use of CH foams wetted by cryogenic DT in order to improve stabilization of Rayleigh–Taylor instability [2–9]. In this frame, two-dimensional studies of shock propagation in foams [10,11] or in array of fibers [12,13] have been done. In AstroPhysics, mass outflows are commonly heterogeneous with wind/cloud interactions. This paper presents what can be seen as an elementary process to be studied in order to achieve a better understanding of the two preceding complex cases.

When a pressure gradient (or step) crosses a mass density gradient (or step) baroclinic vorticity deposition occurs. In the case of pressure and density inhomogeneities (i.e. without any step), this phenomena is described by the vorticity equation: $D_t(\omega/\varrho) = \nabla\varrho \times \nabla p/\varrho^3$ where $\omega = \nabla \times \vec{v}$ is the vorticity, ϱ the matter density, and p the pressure.

As concerns the heterogeneous case (i.e. the shock/interface interaction) previous works have addressed this topic in the frame of semi-infinite media. Henderson addressed in [14] the refraction of a plane shock wave at an oblique interface separating slow/fast or fast/slow media (air–CH_4 or air–CO_2). Transition to irregular refraction pattern is also analyzed in this frame. Samtaney and Zabusky focused in [15] on the baroclinic vorticity deposition at the interface and approximate circulation was calculated for several cases. For planar fast/slow interface, they gave an exact analytical expression of the vorticity deposition as a function of the pressures in the refraction pattern and of the incidence angle of the shock wave.

In this paper, we address the interaction of a strong shock along a two-layer interface in confined geometry. Media and shock are bounded by two rigid walls parallel to the interface. The shock is generated by a rigid piston. Both walls introduce strong constraints of symmetry which make the problem to depart from the usual case of two semi-infinite media. The shock dynamics are compared to the ones of a shock produced by the same piston in an effective homogeneous medium whose density is the average density of the pre-shock flow. As done in the past in foams (see [10,12]), we study the post-shock flow and shock properties which are very different when compared to the effective homogeneous case. In the piston reference frame, vorticity deposition on the interface involves fluid motion whereas an effective homogeneous medium would be static. Confined geometry allows and sustains the existence of a vorticity sheet at the steady state.

The paper is organized as follows. A description of the numerical set-up and of the code we use is given in Section 2. Section 3 is devoted to the early transient stage of the shock propagation while

* Corresponding author.
E-mail address: benoit.canaud@cea.fr (B. Canaud).

0997-7546/$ – see front matter © 2009 Elsevier Masson SAS. All rights reserved.
doi:10.1016/j.euromechflu.2009.04.002

Section 4 focuses on the steady state and stationary irregular refraction at the interface. The post-shock medium in the stationary state is addressed in Section 5. Section 6 contains a study of the shock velocity scaling laws which are compared to the generalized Rankine–Hugoniot relations set from [12] and predicted by mean of a gray-box type model.

2. Numerical set-up

Simulations are done in the piston reference frame. This allows minimum advection of the post-shock fluid. The numerical set-up (see Fig. 1) consists of two layers of densities ϱ_1^0 and $\varrho_2^0 = \eta\varrho_1^0$ with rigid wall boundary conditions at the top, bottom, and left boundaries of the simulation box. At the right boundary, a flux condition is considered. The two layers are initialized with the same velocity u_0 from right to left so that the impact of the fluid on the left wall results in a shock wave propagating from left to right. The fluid velocities are chosen in order to obtain high shock wave mach numbers ($500 < \mathscr{M} < 10000$) relevant for ICF. The fraction of the material of density ϱ_2^0 is ξ and the height of the layer is then $h = \xi L$ where L is the height of the simulation box. The heavy medium density is a free parameter. The box length is chosen to be $30L$. All fluids are considered to be monatomic ideal gases (pressure given by $p = \varepsilon/(\gamma - 1)$ where ε is the specific internal energy, $\gamma = 5/3$). Considering other polytropic coefficients will lead to the same phenomenology as far as the two media are set to have the same polytropic coefficient. The case of two layers with different polytropic coefficients is not addressed here.

The simulation code, called HERA 2D [16], is a hydrodynamics code, developed at the Commissariat à l'Énergie Atomique (CEA). It is a multifluid two-dimensional Eulerian hydrodynamics code with tree-based Adaptive Mesh Refinement (AMR) capability. Its hydrodynamic solver uses a time-explicit Godounov type scheme with interface reconstruction following Young's algorithm [17]. The multi-fluid Euler equations are solved on a Cartesian mesh using a Lagrange and remap scheme together with an alternate direction splitting. After a Lagrangian step, hydrodynamic quantities are projected back onto the fixed Eulerian grid, using a Godlewski method [18].

The code supports various parallel modes, from full MPI to full multithread or hybrid multithread/MPI with dynamic load balancing via subdomain migrations. Implicit thermal conduction, realistic equations of state, and paraxial laser propagation solvers are also available in HERA 2D, but are not used in this study.

Numerical tests have shown that mesh refinement is sufficient to be a non-perturbative parameter. In our simulation, the base grid is 20×600 with 3 levels of refinement by factor 2, which means 160×4800 cells for the full refinement grid. In order to verify our simulation results, we performed simulations for several cases with the same base grid but other refinement parameters (2 levels by factor 2, 2 levels by factor 3, and 3 levels by factor 3). No significant differences were noticed.

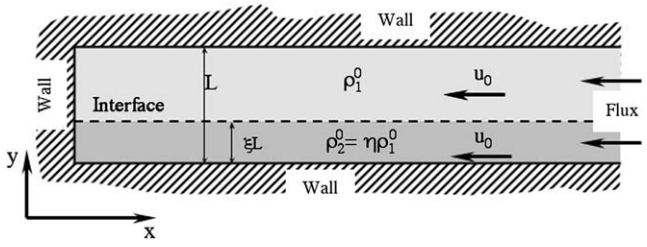

Fig. 1. Numerical set-up of two-layers simulations.

3. Early transient stage

Time evolution can be separated in two different parts: the early transient stage and the steady state. During the transient stage, shock and rarefaction waves travel through the post-shock medium between top and bottom walls while a vortex is forming at the interface.

We recall that for an homogeneous perfect gas, the shock velocity is related to the post-shock fluid velocity by $D_h = (\gamma + 1)u_0/2$ (in the pre-shock fluid reference frame). For a given fluid velocity, pressure in both media behind the shock is given by $(\gamma + 1)\varrho_0 u_0^2/2$, where ϱ_0 is the pre-shock fluid density.

When the layered fluid impacts the wall, a strong planar shock wave is generated orthogonally to the interface in each layer and propagates at the same velocity D_h in both of them. Pressures behind the shock in each material differ by the ratio of their densities. The heavy material then expands in the light one, launching a secondary shock in the latter and a rarefaction wave in the former. Both secondary wave fronts are initially parallel to the walls and refract on the primary (main) shock front. The secondary shock propagating in the light post-shock fluid curves the main shock front and accelerates it. The (secondary) rarefaction wave propagating in the heavy fluid weakens the main shock, decelerating it. A snapshot of the density during this process is presented in Fig. 2. Here, rarefaction wave (rw) and shock wave (sw) can be easily seen. As secondary waves interact with the primary shock, additional waves are emitted in post-shock media from the secondary refraction nodes. The primary shock refraction at the interface becomes irregular. The deflected interface rolls around a large vortex.

The wall boundary conditions reflect all waves, and return them towards the post-shock medium. All of them still act on the primary

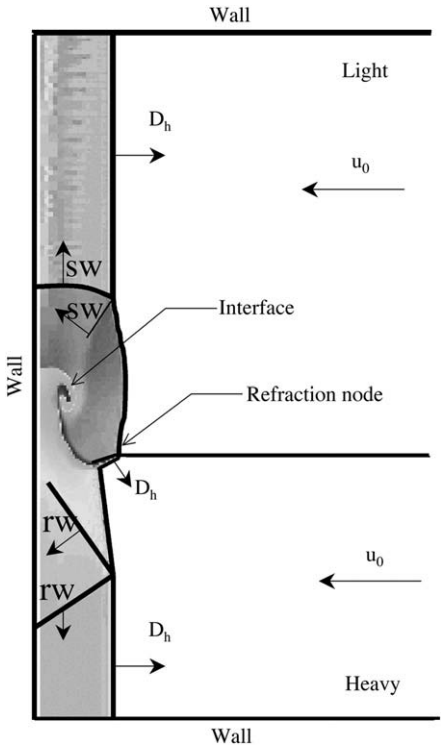

Fig. 2. Early time evolution of fluids. Secondary rarefaction (rw) and shock waves (sw) propagate in post-shock media. Due to baroclinic vorticity deposition, the interface rolls-up and gives birth to a large vortex.

shock front by globally accelerating and decelerating it respectively in the light and heavy medium.

The evolution of the velocity for three specific points of the shock front with respect to the shock velocity in the effective homogeneous case is presented in Fig. 3. The three points are taken at the top (in the light fluid area), at the bottom boundary (in the heavy fluid area), and on the interface (refraction node). At the early times, the lower part of the shock front is slowed while node and upper boundary of the shock front are accelerated.

It is worth stressing that the early transient stage duration is of the order L/D_h, which is the typical time for a shock wave to propagate along the box height L. The shock front evolution in time is displayed in Fig. 4. As the additional waves are reflected on wall boundary conditions and propagate into both media, they get weaker and the shock front evolves to an asymptotic stationary irregular refraction shape.

It is important to note that using different polytropic coefficients for the two materials will initiate shock waves with different velocities in the two materials, possibly leading to a completely different phenomenology (think for example of the case where polytropic coefficients are chosen to achieve the same pressure in the two materials). This case is not considered here.

4. Stationary irregular shock refraction with wall boundary conditions

The steady state is characterized by an average shock velocity larger than the one in the effective homogeneous case, and an irregular refraction pattern. Due to waves traveling behind the shock front, the shock front velocity hovers slightly around the average (see Fig. 2).

The two-dimensional theory of shock wave propagation on an oblique interface in infinite media (see [14,19]), distinguishes two cases of refraction.

If the angle of incidence is under a critical angle, all post-shock flows are supersonic in the shock frame and the shock behavior only depends on the pre-shock flows. This corresponds to the so-called regular refraction case.

If the angle of incidence is over the critical angle, one of the post-shock flows is subsonic. This constitutes the irregular refraction case. Rarefaction waves are emitted at the refraction node and propagate along the shock front toward infinity. The flow then remains non-stationary and the shock front is curved until the refraction reaches a regular state at the node.

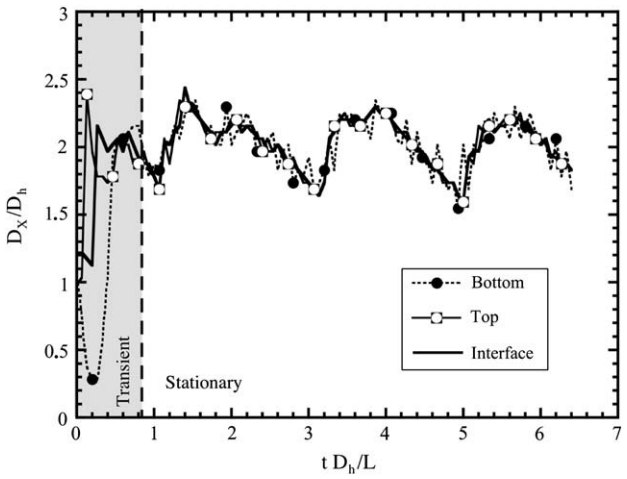

Fig. 3. Shock velocity (upper and lower bounds, refraction node) versus time in post-shock fluid frame.

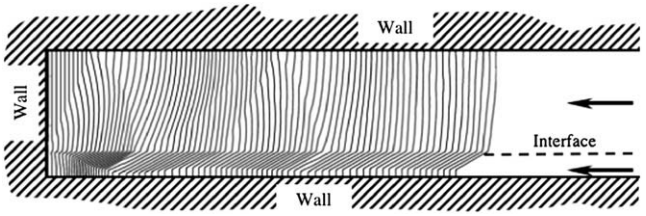

Fig. 4. Shock front at regular time steps.

The case we present in this paper is very different. The wall boundary conditions do not allow waves to propagate to infinity. Those are reflected and constitute a system where the flow becomes nearly stationary. Fig. 5 displays the geometry of our case in the vicinity of the refraction node. α_1 (α_2) is the incidence angle in the light (heavy) material, δ_1 (δ_2) is the deflection angle in the light (heavy) material, and q is the node velocity or apparent shock velocity.

Using shock polar analysis, we can write the equilibrium condition for the interface. The equation of the shock polar is:

$$\tan\delta = \frac{u\sqrt{q^2 - D^2}}{q^2 - Du}, \tag{1}$$

where δ is the deflection angle, u the magnitude of the fluid velocity step, and D the shock velocity magnitude. On the interface, the fluid velocity vectors are colinear so $\delta_1 = \delta_2$, the node velocity q is the same in both materials and pressures on both sides are equal $p_1 = p_2 = p$. Therefore, we consider the intersection of the shock polars in the same plane of parameter q. This intersection stands in the subsonic domain of the light material polar and in the supersonic domain of the heavy material polar. It is an irregular refraction state which stays stationary.

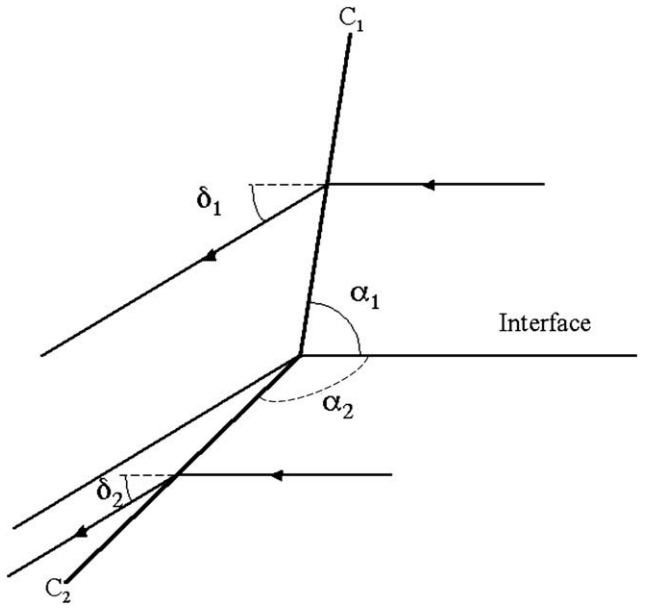

Fig. 5. Wave diagram of refraction in the vicinity of the node. C_1 (C_2) is the shock front, α_1 (α_2) is the incidence angle, and δ_1 (δ_2) is the deflection angle in the light (heavy) fluid.

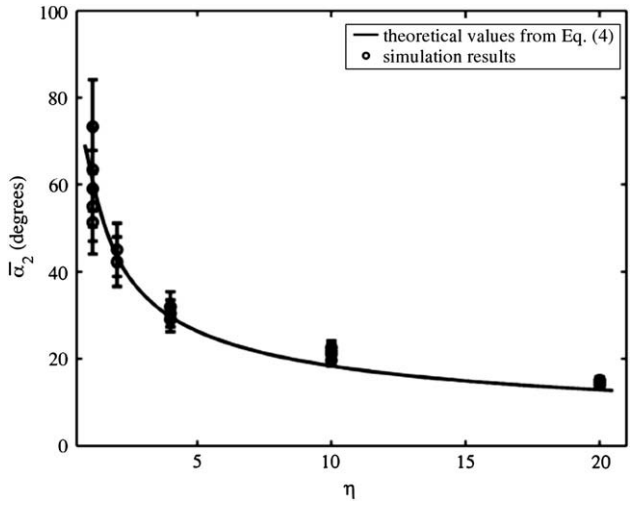

Fig. 6. Incidence supplementary angle $\bar{\alpha}_2 = (\pi - \alpha_2)$ versus η from Eq. (4) (plain line) and numerical simulations (dots).

Using the Hugoniot relations for strong shocks and equating $\delta_1 = \delta_2$ in Eq. (1) leads to a third degree equation. Excepting the trivial solution $p = 0$, the two solutions are:

$$p = \frac{\varrho_2^0 q^2(\gamma+1)(\eta+1)}{4\gamma\eta}\left(1 \pm \sqrt{1 - \frac{16\gamma\eta}{(\gamma+1)^2(\eta+1)^2}}\right). \tag{2}$$

The solution with the plus sign leads to a negative term under the square root in Eq. (1) and is not relevant. Eq. (2) gives the pressure p at the refraction node as a function of q. As the post-shock flow of the heavy fluid is supersonic, p is also the pressure in the post-shock heavy fluid.

Considering the incidence angles α_1 and α_2, with the geometric relation $q = D/sin\alpha$, we obtain:

$$\sin\alpha_1 = \frac{(\gamma+1)}{2}\sqrt{\frac{\eta+1}{2\gamma}\left(1 - \sqrt{1 - \frac{16\gamma\eta}{(\gamma+1)^2(\eta+1)^2}}\right)}, \tag{3}$$

$$\sin\alpha_2 = \frac{\sin\alpha_1}{\sqrt{\eta}}. \tag{4}$$

These relations are of great interest as they show that the angles only depend on η. Using Eq. (2) in Eq. (1), we can also prove that the deflection angle $\delta_1 = \delta_2$ only depends on η.

In the case $\eta = 1$, the intersection of the polars is located on the sonic point. The two angles α_1 and α_2 are equal to the sonic angle, and the shock front is straight. This corresponds to a homogeneous medium case.

If we consider the limit $\eta \to \infty$, we get from Eqs. (3), (4) and (2): $\alpha_1 = \pi/2$, $\alpha_2 = \pi$, and $p = \varrho_1^0 q^2 2/(\gamma+1)$. In this case, the heavy medium behaves like a wall (infinite density) and we recover the one-dimension shock propagation in the light medium. The limit $\eta = 0$ is essentially the same when inverting the role of the two media.

Actually, for $\eta > 2$, we can consider that $\alpha_1 \approx \pi/2$. This mean that the shock remains nearly straight in the light material so that the pressure right behind the shock front is roughly constant defining a buffer area.

As displayed in Fig. 6, the relation stated in Eq. (4) is well verified. Error bars come from the grid refinement. Measuring p, α_1, δ_1, or δ_2 on the simulation results will lead to much larger error bars due either to the pressure fluctuations (for p), to shock front curvature (for α_1, δ_1) or to the smallness of the angle (for δ_2).

5. Shear layer and buffer area characterization

When the steady state is reached, right behind the shock front, the fluid is sheared along the deflected interface. The post-shock heavy fluid is reflected by the bottom wall and advected back to the left one, forming several arches. These arches constitute a layer at the bottom of the post-shock medium. The left wall reflects the fluid back to the shock front, forming another layer at the top of the box. An example of density and velocity maps is given in Fig. 7.

The post-shock flow can be separated into two different parts: a buffer zone and a shear layer.

In the shear layer, the basic flow velocity u has the classical form from [20,21], namely: $u = \tanh y$. More generally, the exact nonlinear solution of the inviscid equation of motion, which is called two-dimensional, coherent shear layer vortex, and known as Stuart vortex (see [22]), is the stream function defined by:

$$\psi = \log\left[C\cosh y + \left(C^2 - 1\right)^{1/2}\cos x\right]. \tag{5}$$

where $C \in [1, \infty]$ is a parameter describing the nature of vortices layer ($C \to 1_+$ corresponds to an unperturbed plane mixing layer and $C \to \infty$ to a row of point vortices). Longitudinal (along x) and transverse (along y) velocities are defined respectively by: $u = \partial_y\psi$ and $v = \partial_x\psi$. In our problem, C is close to 1 and the mean velocity $< u >$, averaged over the total thickness of the shear layer and over a wide time interval, can be approached by:

$$< u > = \sum_i C_i \tanh(k_i(y - y_i)), \tag{6}$$

where k_i has a wave-vector dimension.

The velocity $<u>$, calculated numerically for five values of the ξ parameter and $\eta = 4$, is shown on Fig. 8. In the same plot, fits of numerical results by Eq. (6) are presented with dashed lines.

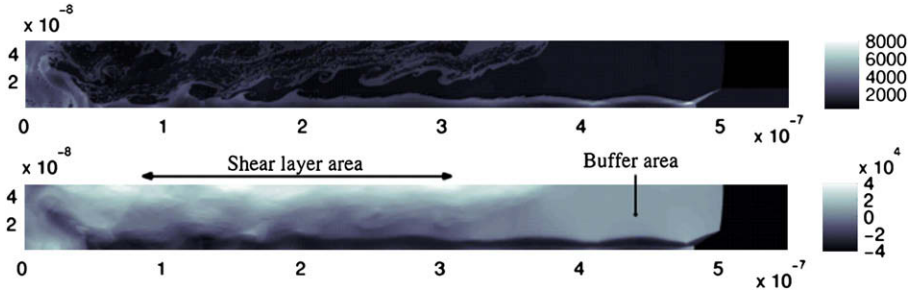

Fig. 7. Maps at steady state for the case $\xi = 0.3$, $\eta = 4$ (top: density in kg m^{-3}, bottom: longitudinal fluid velocity in m s^{-1}).

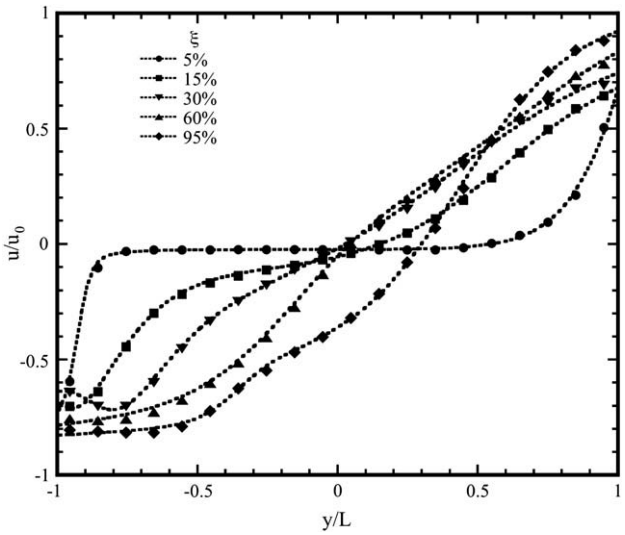

Fig. 8. Longitudinal velocity versus transverse abscissa, for different values of ξ, with $\eta = 4$. Numerical results are dots, triangles, squares, and diamonds.

Here, numerical data are accurately described by a sum of three tanh y-functions.

Vorticity sheet with $C = 1$ is an unstable solution of fluid equations. However, wall boundary conditions allow one to sustain such a solution.

A coupling between the shear layer and the shock front is realized via the subsonic part of the post-shock flow ("buffer area") located in the upper part of the box. In this area, fluid velocity, density, and pressure are nearly homogeneous.

6. Shock velocity scaling laws

When the refraction at the interface becomes irregular, the main shock is accelerated and its velocity becomes higher than the shock velocity in the effective homogeneous medium. It is interesting to study the relative deviation of the shock velocity $\Delta q/q_h = (q - q_h)/q_h$, where $q_h = D_h$ is the shock velocity in the effective homogeneous medium.

Starting from Eq. (2) and dividing by p_h, the pressure of the post-shock material in the homogeneous case, we can write $\Delta q/q_h$ as a function of ξ, η, and p/p_h:

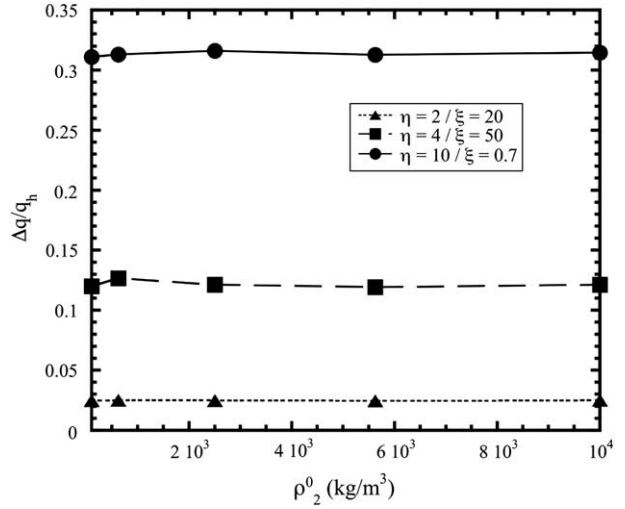

Fig. 9. $\Delta q/q_h$ as function of ϱ_2^0 for three different cases.

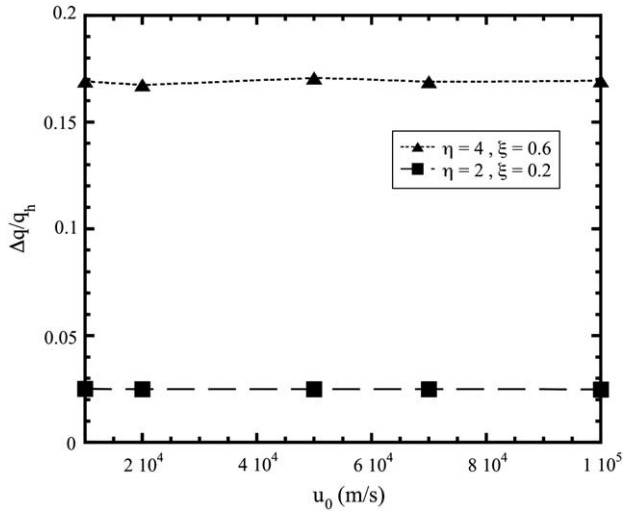

Fig. 10. $\Delta q/q_h$ as function of u_0 for two different cases.

$$\frac{\Delta q}{q_h} = \sqrt{\frac{\frac{1-\xi}{\eta} + \xi}{\sin^2 \alpha_2} \frac{p}{p_h}} - 1. \tag{7}$$

p/p_h is related to the ratio of internal energies in the two-layer case and effective homogeneous medium.

$\Delta q/q_h$ does not depend on ϱ_2^0 and u_0, as can be seen in Figs. 9 and 10.

Hazak et al. derived generalized Rankine–Hugoniot in [12] for the case of a regular array of fibers. It consists in averaging the mass, momentum, and energy conservation laws in a box in a way that nullifies the flux orthogonal to the direction of propagation and such that the mean velocity along the box remains constant. The main result consists in the following relations:

$$\langle\langle \varrho \rangle\rangle q = \varrho_h q + \langle\langle \varrho u_x \rangle\rangle, \tag{8}$$

$$\langle\langle \varrho u_x \rangle\rangle q - \left\langle\left\langle \varrho u_x^2 \right\rangle\right\rangle = \langle\langle p \rangle\rangle, \tag{9}$$

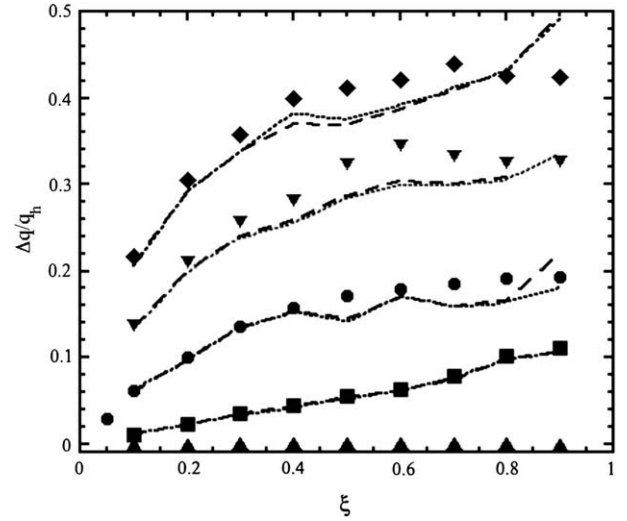

Fig. 11. $\Delta q/q_h$ vs. ξ for $\eta = 1.1$ (triangles), 2 (squares), 4 (dots), 10 (reversed triangles), and 20 (diamonds) estimated numerically. Dotted and dashed lines represent $\Delta q/q_h$ deduced from respectively Eqs. (8) and (9).

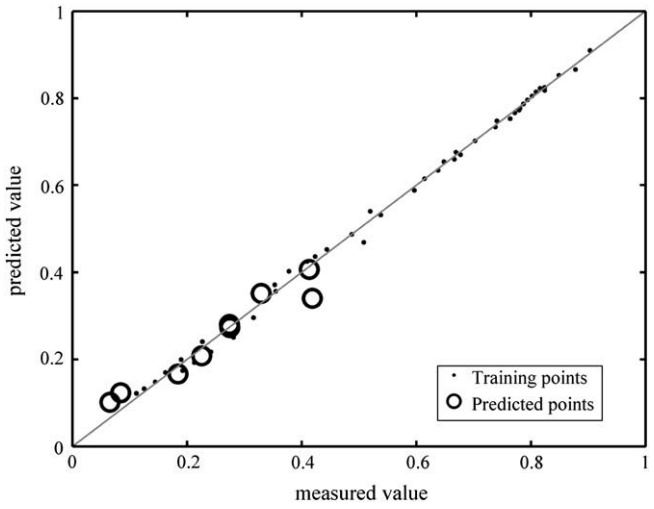

Fig. 12. Measurement versus predicted value for model training points and for validation (predicted) points.

$$\frac{1}{2}\left\langle\left\langle \varrho u_x^2 \right\rangle\right\rangle q + \frac{1}{\gamma-1}\langle\langle p\rangle\rangle q - \frac{1}{2}\left\langle\left\langle \varrho u_x^3 \right\rangle\right\rangle - \frac{1}{\gamma-1}\langle\langle p u_x\rangle\rangle = \langle\langle p u_x\rangle\rangle. \tag{10}$$

In the case of shock propagation along the two-layer setup, a similar approach can be made. The generalized Rankine–Hugoniot relations (cf. Eqs. (8) and (9)) allow to compute the shock velocity deviation $\Delta q/q_{\mathrm{h}}$ using the numerical hydrodynamic quantities averaged over a $L \times L$ area located right behind the shock front. The resulting $\Delta q/q_{\mathrm{h}}$ is also time averaged. Results of these calculations agree with the measurements, as shown in Fig. 11.

Unfortunately, no analytical expression of the coupling between the post-shock pressure p/p_{h} and the input parameters ξ and η is known.

In order to construct a predictive model, we use a multi-layer neural network (see for instance [23]) to get p/p_{h} as a function of ξ and η. The network is constituted by 3-tanh perceptrons in a hidden layer and a purely linear perceptron as output neuron. Training is done by Levenberg–Marquardt gradient back-propagation. An example of the explicit form reads as:

$$\frac{p}{p_h} = b + W^{(2)} \cdot \tanh\left(W^{(1)} \cdot \Xi\right), \tag{11}$$

where

$$W^{(1)} = \begin{bmatrix} -1.2031 & -0.71544 & -0.17606 \\ -0.9222 & -0.47136 & -0.17003 \\ 0.21256 & 1.7428 & 0.023738 \end{bmatrix}; \Xi = \begin{bmatrix} 1 \\ \xi \\ \eta \end{bmatrix} \tag{12}$$

$$W^{(2)} = [-36.5805 \quad 20.3398 \quad -1.2356]; b = -14.9117$$

The resulting model appears to be well predictive (cf. Fig. 12), even outside of the training η domain.

7. Conclusion

Direct numerical simulations of shocks propagating along a two-layer interface confined between two walls parallel to it are presented. This very singular case can be seen as an elementary process to be understood before addressing more complex heterogeneous media such as arrays of fibers or wetted foams. It also constitutes an interesting case by itself which allows very strong vorticity deposition and shock velocity that differs significantly from the one in a homogeneous media of the same average density. The choice of this specific numerical set-up gives an opportunity to characterize the stationary irregular refraction pattern which occurs in confined geometry.

It is seen that this refraction pattern is achieved after a transient stage during which numerous shock replicas shape the primary shock front. In the post-shock flow a vorticity sheet takes place where fluid motion stores kinetic energy.

A generalized set of Rankine–Hugoniot relations for average of hydrodynamic quantities is shown to be verified and explains in which way this so-called "anomalous" kinetic energy storage is related to shock velocity. Model for the coupling between pressure at the refraction node and input parameters is still needed, and it is shown that this can be predicted by means of a neural network.

Acknowledgments

The authors would like to thank H. Jourdren, D. Dureau and S. Jaouen for their help for Hera support, and L. Brun, L. Soulard, J.-F. Haas, N. Lecler, R. Quach and A. Decoster for fruitful discussions.

Refs

[1] B. Canaud, X. Fortin, F. Garaude, C. Meyer, F. Philippe, M. Temporal, S. Atzeni, A. Schiavi, Nucl. Fusion 44 (2004) 1118.
[2] B. Canaud, F. Garaude, P. Ballereau, J. Bourgade, C. Clique, D. Dureau, M. Houry, S. Jaouen, H. Jourdren, N. Lecler, et al., Plasma Phys. Contr. Fusion 49 (2007) B601.
[3] B. Canaud, F. Garaude, C. Clique, N. Lecler, A. Masson, R. Quach, J.V. der Vliet, Nucl. Fusion 47 (2007) 1652.
[4] R. Sacks, D. Darling, Nucl. Fusion 27 (1987) 447.
[5] S. Bodner, D. Colombant, A. Schmitt, M. Klapisch, Phys. Plasmas 7 (2000) 2298.
[6] S. Skupsky, R. Betti, T. Collins, V. Goncharov, D. Harding, R. McCrory, P. McKenty, Inertial Fusion Science and Applications (2001) 240.
[7] T. Takeda, K. Mima, T. Norimatsu, H. Nagatomo, A. Nishiguchi, Inertial Fusion Science and Applications (2001) 250.
[8] T. Norimatsu, K. Nagai, T. Takeda, T. Yamanaka, Inertial Fusion Science and Applications (2001) 752.
[9] S. Bodner, D. Colombant, A. Schmitt, J.H. Gardner, R. Lehmberg, S. Obenschain, Fusion Eng. and Design 60 (2002) 93.
[10] F. Philippe, B. Canaud, X. Fortin, F. Garaude, H. Jourdren, Las. Part. Beam 22 (2004) 171.
[11] T.J.B. Collins, A. Poludnenko, A. Cunningham, A. Frank, Phys. Plasmas 12 (2005) 062705.
[12] G. Hazak, A. Velikovich, J. Gardner, J. Dahlburg, Phys. Plasmas 5 (1998) 4357.
[13] D. Kotelnikov, Montgomery, Phys. Fluids 10 (1998) 2037.
[14] L.F. Henderson, J. Fluid Mech 26 (1966) 607.
[15] R. Samtaney, R. Zabusky, J. Fluid Mech 269 (1994) 45.
[16] H. Jourdren, Lecture Notes in Computational Science and Engineering, Vol. 41, Springer, Berlin, 2005.
[17] D. Youngs, Technical report, AWRE Design Mathematics Division, AWRE/44/92/35, 1992.
[18] E. Godlewski, P.A. Raviart, Numerical Approximation of Hyperbolic Systems of Conservation Laws, Vol. 118, Springer, 1996.
[19] J. Thouvenin, Détonique, Eyrolles, Paris, 1997.
[20] R. Betchov, A. Szewczyk, Phys. Fluids 6 (1963) 1391.
[21] R.E. Kelly, J. Fluid Mech 27 (1967) 657.
[22] J.T. Stuart, J. Fluid Mech 29 (1967) 417.
[23] J. Hertz, A. Krogh, R. Palmer, Introduction to the Theory of Neural Computation, Addison Wesley, 1991.